Optical mapping of ground reaction force dynamics in freely behaving *Drosophila melanogaster* larvae

Jonathan H. Booth[1,2,3], Andrew T. Meek[1,2], Nils M. Kronenberg[1,2], Stefan R. Pulver[3]*, and Malte C. Gather[1,2]*

[1]SUPA, School of Physics and Astronomy, University of St Andrews, Fife, United Kingdom; [2]Humboldt Centre for Nano- and Biophotonics, Department of Chemistry, University of Cologne, Germany; [3]School of Psychology and Neuroscience, University of St Andrews, Fife, United Kingdom.

* equal contribution; correspondence: sp96@st-andrews.ac.uk, mcg6@st-andrews.ac.uk

Abstract

During locomotion, soft-bodied terrestrial animals solve complex control problems at substrate interfaces, but our understanding of how they achieve this without rigid components remains incomplete. Here, we develop new all-optical methods based on optical interference in a deformable substrate to measure ground reaction forces (GRFs) with micrometre and nanonewton precision in behaving *Drosophila* larvae. Combining this with a kinematic analysis of substrate interfacing features, we shed new light onto the biomechanical control of larval locomotion. Crawling in larvae measuring ~1 mm in length involves an intricate pattern of cuticle sequestration and planting, producing GRFs of 1-7 µN. We show that larvae insert and expand denticulated, feet-like structures into substrates as they move, a process not previously observed in soft bodied animals. These 'protopodia' form dynamic anchors to compensate counteracting forces. Our work provides a framework for future biomechanics research in soft-bodied animals and promises to inspire improved soft-robot design.

Keywords: *Drosophila* | mechanobiology | biomechanics | locomotion | kinematics | soft-bodied | larvae | ground reaction force | protopodia | ERISM | WARP

Introduction

Locomotion is a fundamental behaviour in the Animal Kingdom. There is great diversity in how it is accomplished, from the modification of torque angles in rigid bodied animals (Audu et al., 2007) to a diverse array of peristalses in limbed (reviewed in van Griethuijsen & Trimmer, 2014) and limbless soft-bodied animals (Berrigan & Pepin, 1995). Key to these different strategies is one unifying characteristic: action against a substrate or fluid produces forces, thereby translating the body in space. In an aquatic environment, forces acting within fluids can be visualised via the waves of distortion they cause, thus facilitating the development of detailed theories of movement (Gray & Lissmann, 1964). In terrestrial settings, however, substrates are often rigid and therefore prevent direct visualisation of the ground reaction forces (GRFs) generated by animals.

Interactions with substrates have been extensively studied in animals with articulating skeletons (i.e. rigid bodied animals) due to the ability to calculate output forces from lever physics combined with measurements of joint-angles (Audu et al., 2007; Bobbert et al., 2007). However, much less is known about substrate interactions and GRFs in soft-bodied animals without internal or external skeletons. These animals lack articulating joints upon which muscles act, ambiguating points through which the animal interacts with the substrate. However, they too must anchor a part of their body when another part is in motion to prevent net progression being impeded by an equal but opposite reaction force, i.e. their movements must obey Newton's 3rd law of motion (Trueman, 1975). Furthermore, controlling soft bodies is difficult because they have highly non-linear physical properties and virtually unlimited degrees of freedom. Movement over terrain therefore presents a unique challenge for soft animals. Dynamic anchoring has long since been postulated to be at the heart of soft-bodied locomotion (Tanaka et al., 2012), but understanding the mechanisms by which soft animals achieve this remains an open problem. Prior work on caterpillars (Lin & Trimmer, 2010; Lin et al., 2011; Lin & Trimmer, 2012), leeches (Cacciatore et al., 2000; Kampowski et al., 2016) and *C. elegans* (Fang-Yen et al., 2010; reviewed in Gjorgjieva et al., 2014) provided key insights and inspired development of soft robots (Lu et al., 2018; Zhang et al., 2009; reviewed in Kim et al.,

2013); however, a lack of methods with sufficient spatiotemporal resolution for measuring GRFs in freely behaving animals has limited progress.

Many advances in cellular mechanobiology have been fuelled by the development of new force measuring techniques that allow optical measurement of GRFs (reviewed in Mohammed et al., 2019). For example, Elastic Resonator Interference Stress Microscopy (ERISM) (Kronenberg et al., 2017a) and a variant, Wavelength Alternating Resonance Pressure microscopy (WARP) (Meek et al., 2021) enable optical mapping of GRFs in the nanonewton range with micrometre and millisecond precision by monitoring local changes in the optical resonances of soft and deformable microcavities, including in very small, low force structures (Dalaka et al., 2020).

In parallel, great strides have been made in understanding the neural and genetic underpinnings of locomotion in the *Drosophila* larva (Fushiki et al., 2016; Heckscher et al., 2012; Pulver et al., 2015; Schneider-Mizell et al., 2016; Zwart et al., 2016), a genetically tractable soft-bodied model organism (Mantziaris, Bockemühl and Büschges, 2020; reviewed in Clark et al., 2018). *Drosophila* larvae are segmentally organised peristaltic crawlers that move by generating waves of muscle contractions (Berrigan & Pepin, 1995). Larvae have segmentally repeating bands comprised of 6 rows of actin trichomes (denticles) (reviewed in Payre, 2004). The developmental and genetic origins of these structures have been extensively studied, but relatively little is known about how they are articulated during movement. While computational modelling and biomechanical measurements have provided an initial knowledgebase (Khare et al., 2015; Loveless et al., 2019, 2020; Sun et al., 2022), data on biomechanical forces generated during substrate interactions in *Drosophila* larvae remain extremely limited (Khare et al., 2015; Sun et al., 2022; Tytell et al., 2011). Development of methods for measuring GRFs in this model organism would enable fully integrated neurogenetic-biomechanical approaches to understanding soft-bodied movement.

Here, we develop ERISM and WARP based approaches to measure GRFs exerted by freely behaving *Drosophila* larvae. We combine these measurements with kinematic tracking to explore how soft-bodied animals overcome fundamental biophysical challenges of moving over terrain. We find that, despite their legless appearance,

Drosophila larvae interact with substrates by forming and articulating foot-like cuticular features (‘protopodia') and cuticular papillae, which act as dynamic, travelling anchors. The use of ERISM-WARP provides a step-change in capability for understanding how soft-bodied animals interact with substrates and paves the way for a wider use of optical force measurement techniques in animal biomechanics and robotics research.

Results

Kinematic tracking of substrate interfacing features

As a first step in understanding how larvae interact with substrates, we confined 3rd instar larvae to glass pipettes lined with soft agarose (0.5% w/v) (**Figure 1A**). This allowed us to laterally image the animals and the lateral edges of denticle rows at the substrate interface (**Figure 1B**) while animals crawled towards an appetitive odour source. Animals interact with the substrate by large, soft, segmentally repeating cuticular features that contain rows of denticles and to which we refer as ‘protopodia' in the following. Protopodia in each segment engaged in ‘swing’ periods (moving, SwP) and ‘stance’ periods (planted on substrate, StP) as waves propagated through the body. During SwPs, protopodia detached from the substrate, with the posterior row of denticles moving to meet the anterior row of denticles, thereby inverting the cuticle and sequestering the whole protopodia into a travelling pocket (**Figure 1C**). When protopodia ended their SwP, they unfolded from the sequestration pocket and then protruded into the substrate during the StP.

To further investigate the dynamics of protopodia placements, we performed detailed kinematic tracking of the morphometry of protopodia, denticle bands, and inter-protopodial spaces during peristaltic waves. By tracking the movement of defined points on bands relative to each other, we monitored intersegmental and intra-segmental movements during peristaltic waves (**Figure 2A**). In addition to moving relative to each other, denticle bands changed their shape during the sub-phases of a peristaltic wave. During forward waves (peristaltic contractions travelling in an anterograde direction), the anterior-most row of each denticle started to move after the corresponding posterior-most row (**Figure 2B**) and completed its movement after the posterior-most row stopped moving (**Figure 2C**), i.e. there was an anteroposterior (AP) latency for both Swing

Initiation (SI) (when movement begins) and for Swing Termination (ST) (when movement ends). Such a ‘rolling’ progression pattern is analogous to the ‘heel-to-toe' footfalls of limbed animals (reviewed in Federle & Labonte, 2019). To analyse this pattern further, we quantified the percentage of the wave duration spent in AP latency during SI and ST. For forwards waves, this relative latency was generally consistent across the denticle bands on large protrusive protopodia but less pronounced for the smaller and less protruding protopodia at the extreme posterior and anterior abdomen and the thorax (**Figure 2D**). In backwards waves, the heel-toe like latency was reversed, with anterior-led latencies observed in SI and posterior-led latencies observed in ST (**Supplementary Figure S1**).

In summary, each segment-wise denticle action event is composed of four distinct periods: SI, SwP, ST, and StP. For forward waves and posterior segments, the latencies during the SI period are strongly correlated to wave duration (R^2 range: 0.46-0.78, A7-A4) but not for anterior abdomen and thorax (R^2 range: 0.12-0.35, A3-A1 and T3, **Figure 2E**). The magnitudes of ST-related latencies are not strongly correlated across most segments (R^2 range: 0.01-0.26, **Figure 2F**).

Developing stress microscopy for *Drosophila*

Kinematic analysis of protopodia movements revealed a previously uncharacterised complexity in the dynamics of larval movement, but it cannot quantify the mechanical forces impacting the substrate. To achieve this, we therefore adapted ERISM-WARP (**Figure 3A**, **Supplementary Figure S2**) to map the GRFs exerted by larvae rather than the forces exerted by single cells. First, we developed optical microcavities with mechanical stiffnesses in the range found in hydrogel substrates commonly used for studying *Drosophila* larval behaviour, i.e. Young’s modulus (E) of 10-30kPa (Ahearne et al., 2005; Apostolopoulou et al., 2014; Salerno et al., 2010). These microcavities consisted of two semi-transparent, flexible gold mirrors sandwiching a transparent polymer rubber that was made from a mixture of siloxanes with discrete Young’s moduli to adjust the resulting stiffness (Palchesko et al., 2012). The microcavities were characterised using atomic force microscopy (AFM) and the resulting force distance curves (**Figure 3B**) were fitted to a height-corrected Hertz Model to determine the

Young's modulus of each cavity (Dimitriadis et al., 2002). This procedure allowed us to fabricate microcavities with a wide range of well-defined Young's moduli (**Figure 3C**, **Supplementary Table 1**).

As an initial test, we placed cold-anaesthetised 2nd instar larvae onto a microcavity (E=28kPa) and performed ERISM force mapping at different magnifications to record substrate indentations generated by larval body features (**Figure 3D-L**). Indentation maps were computed from the images of optical interference by pixelwise solving of the resonance condition with an optical model. Stress maps were then computed from the indentation maps via a finite element method (FEM) simulation of the stress distribution required to produce the observed indentation profile (Methods; the accuracy of our calculations was confirmed applying a known force with an AFM, **Supplementary Figure S5**). With this approach, we were able to resolve indentations from rows of denticle bands interdigitated by naked cuticle (**Figure 3G-I**). At higher magnification and when using slightly softer microcavities (E=19kPa), even indentations from individual denticles within these bands were resolved (**Figure 3J-L**). The median force exerted by individual denticles was 11.51nN (1.4nN-47.5nN; n=130 denticles) across a median area of 2.81µm (1.15-9.13µm; n=130 denticles).

Videorate force mapping in freely behaving animals

Next, we moved to force mapping of freely behaving animals. First, we confirmed that ordinary larval behaviour is maintained on collagen-treated microcavity substrates (**Supplementary Figure S3**). We then adapted WARP (Meek et al., 2021) to image substrate interactions at high temporal resolution (**Supplementary Figure S4)**. For forward peristaltic waves, we observed posterior to anterior progressions of indentations into the cavity, corresponding to protopodial placements (**Figure 4A**). We also observed upward deflections of the substrate (i.e., increase in microcavity thickness, positive stress), associated with the displacement of elastomer because of Poisson's ratio governing elastic materials (Pritchard et al., 2013). During StP, protopodia displaced the substrate, and during SwP, protopodia local to the contraction were completely removed from the substrate while travelling to their new resting position.

We also used WARP to investigate the bilaterally asymmetric head sweeps generated by *Drosophila* larvae to sample odours and direct navigation. During head sweeps, anterior segments and mouthhooks detached or dragged across the substrate before replanting (**Figure 4B**). 0.5-1s prior to headsweep initiation, the contact area in posterior segments increased, spreading outwards laterally, employing both the protopodia and the naked cuticle along the midline (**Figure 4C**). This broad but shallow anchoring quickly returned to the ordinary resting phase profile after the mouth hooks were replanted onto the substrate (**Figure 4D**).

Before forwards waves and headsweeps, larvae produced large indentations posterior to their terminal segment. Anatomical examination revealed accessory structures located at the terminus of the posterior abdomen. Together with the terminal denticle band, these cuticular processes generated tripod-shaped indentation patterns (**Figure 4E**). The left and right sides of the tripod deployed and detached simultaneously (**Figure 4F**). Tripod formation was seen before all observed forwards waves (n=28 across 6 animals) and bilateral thoracic activity (n=3 across 2 animals), but not all tripod contacts resulted in further behaviour (**Figure 4G**). To investigate the relationship between tripod placement and locomotion further, we recorded the delay between tripod contact and protopodial detachment in A7. The mean delay was 0.66s±0.21s (**Figure 4H**, n=20 waves across 6 animals).

Next, to estimate the GRF associated with the indentation of each protopodium, we integrated the displacement and stress maps over the region covered by each protopodium. During forward waves, the temporal evolution of GRFs mirrored the characteristics of the cycle seen in the stress maps, with absolute GRFs ranging between 1 and 7μN (**Figure 5A**). However, unexpectedly, we observed an additional force on the substrate when protopodia leave the substrate (SI) and when they are replanted (ST). To investigate whether this force was due to an active behaviour or due to shifting body mass, we plotted integrated displacement (i.e. displaced volume) against the contact area for each protopodium, combining data from multiple forwards waves (**Figure 5B**). Area is correlated with displaced volume for most time points, indicating that volume is a

consequence of mass in a 2nd order polynomial relationship. Comparing different animals, we find that GRFs were relatively consistent across most segments (**Figure 5C**).

The contact area of each protopodium showed a pronounced peak during SI and ST. The maximum contact area during ST was significantly greater than during SI for the posterior abdomen ($p \leq 0.05$ for A8/9-A3) but not for the anterior abdominal protopodium ($p > 0.05$ for A2) (**Figure 5D**). The peak of the displaced volumes during SI was positively correlated with wave duration (R^2 range: 0.48-0.69, A7-A4, **Figure 5E**), again except for the anterior abdomen (A3: $R^2=0.15$; A2: $R^2=0.24$). However, the peak of the displaced volumes during ST was not well correlated with wave duration (R^2 range: 0.03-0.05, A7-A2). This suggests that protopodia push off from the substrate harder during faster waves, but that wave speed does not influence protopodial placement. This observation is consistent with our morphometric data, which showed that wave duration is associated with SI latencies but not with ST latencies.

Sub-protopodial force dynamics

Lastly, to investigate how forces are translated into the substrate within a single protopodium during a 'footfall' cycle, we examined the spatiotemporal substrate interaction during the ST (**Figure 6A**). This showed how protopodia expand their indentive contact across both the AP and mediolateral (ML) axes when being replanted. Kymographs along the AP midline of animals and profiles running up the AP axis extracted from these revealed a delay between when the most posterior and the most anterior part of the protopodium contacts the substrate (**Figure 6B**). The mean contact delay relative to the most posterior part of the protopodium was 0.035s±0.007s at 6µm away from the most posterior part and increased to 0.062s±0.021s and 0.253±0.115s in the middle and at the most anterior part of the protopodium, respectively (**Figure 6C**).

To examine how protopodia expand along the ML axis, we performed a similar analysis, taking kymographs and profiles for the displacement maps at different distances to the midline of a protopodium. At a medial distance from the midline, the contact delay relative to the midline was 0.045s±0.022s (left) and 0.057s±0.019s (right). At the distal left and right of the protopodium, contact occurred 0.111s±0.030s (left) and 0.165s±0.058s (right) after midline contact (**Figure 6D**). This analysis also showed that protopodia insert a

medial-spike into the substrate, through which ST related peak GRFs are conferred, before expanding along the AP and ML axes.

Discussion

Drosophila larvae, though legless, have protopodia

The cuticle of larvae shows distinct patterns of denticulation (denticle bands) and the developmental processes which give rise to these features have been well studied (reviewed in Payre, 2004). Here, we show that denticle bands are situated upon larger articulated foot-like cuticular processes, which act as locomotory appendages. Protopodia dynamically change shape during locomotion, allowing sequestration and presentation of denticles. Individual protopodia and individual denticles exert GRFs in the 1-7µN and 1-48nN ranges, respectively. Superficially, protopodia resemble the much smaller pseudopodia in cells – transient structures, similarly covered with actin protrusions, used by cells to facilitate movement (Burnette et al., 2014). Protopodia may underlie ‘creeping welts’ noted in larger dipteran larvae (Friesen et al., 2015) and show similarities to soft prolegs of *Manduca sexta* caterpillars but are approximately 30 times smaller (Lin & Trimmer, 2010).

Insights from morphometric kinematic tracking of denticle band movements

Our study provides the first detailed description of the morphometry of denticle bands during movement, showing how denticle bands are deployed onto and removed from the substrate. Posterior denticle rows hit the substrate before anterior rows during deployment (ST) and left the substrate before anterior rows during removal (SI). This suggests that both deployment and removal involved rolling ‘heal-toe’ like movements, similar to footfalls in limbed animals, including terrestrial arthropods (reviewed in Federle and Labonte, 2019). Removal but not deployment correlated with wave duration. In *Manduca* caterpillars, it has been noted that SwPs scale positively with wave duration (Simon et al., 2010); however, to our knowledge there is no measurement for SI and ST in these animals.

SI latencies were much more strongly correlated with wave duration across most segments than ST latencies. SIs scale with SwP and this could be mediated by

proprioceptor activity in the periphery (Vaadia et al., 2019). Fine sensorimotor control of musculature during this process would allow for precisely tuned propulsion during peristalsis. In contrast, the more random nature of the ST suggests the process is less finely controlled. This could be a consequence of fluid inertia within the animal, and/or the release of elastic energy from cuticle (Sun et al., 2022) or relaxation of muscles (Ormerod et al., 2022; Simon et al., 2010).

ERISM-WARP allows computation of ground reaction forces in *Drosophila* larvae

We adapted state-of-the-art mechanobiological force measuring techniques to enable measurement of substrate interaction dynamics of a freely behaving soft-bodied animal with micrometer spatial resolution, millisecond temporal resolution and nanonewton force resolution. Previously, high-resolution force mapping was limited to cellular mechanobiology. Specifically, we developed microcavity resonators tuned to the forces generated by larvae and employed ERISM and WARP to perform direct measurements of substrate interactions in anesthetized and behaving animals. GRFs produced by individual denticles in anaesthetised animals were in the ~11nN range. The measured vertical GRFs produced by the individual protopodia of each segment were in the 1 to 7µN range, roughly three orders of magnitude less than the 17mN recorded from an entire 1.72g *Manduca sexta* caterpillar (Lin & Trimmer, 2010). Our measurements provide fundamental constraints for future biomechanical modelling studies seeking to incorporating these structures.

Displacement and stress maps produced during larval crawling revealed that animals can control when and how protopodia contact the substrate. During forward waves, protopodia detached completely during SwP. This observation, coupled with our lateral imaging of protopodia in constrained animals, explains how larvae prevent their rough denticulated cuticle from creating drag due to friction against the direction of the wave. Larvae do not simply pull protopodia off the substrate in a vertical direction; instead, they horizontally slide posterior regions forward in the axis of travel, before sequestering friction generating features (denticles). This shows similarities to the use of shearing forces to detach adhesive pads in limbed arthropods (reviewed in Federle and Labonte, 2019). Inversion of the cuticle to remove denticles from the substrate may also explain

why natural variations in denticle count across animals do not strongly affect locomotor behaviour (Fitzpatrick & Szewczyk, 2005). The invagination process is reversed in order to expand the protopodia into and locally across the substrate, providing an expanding anchor which can serve as a postural support to enable locomotion and prevent lateral rolling during bilaterally asymmetric behaviours such as head sweeps. The dynamic anchoring during the progression of peristaltic waves thus serves to counteract horizontal reaction forces resulting from Newton's 3rd law of motion. Such a sequence of positioning points of support and anchoring them against the substrate has long been postulated to be a fundamental process in soft-bodied locomotor systems (Trueman, 1975); and may be central to explaining why soft-bodied animals have evolved segmentally repeating bodies (Budd, 2001).

Our ERISM-WARP measurements also revealed substrate interaction from accessory structures. Immediately before enacting headsweep, larvae redistributed their body mass into naked cuticle in between protopodia along the midline, effectively fusing multiple protopodia into a single 'ultra-protopodia' that extends across multiple posterior segments. This redistribution occurs hundreds of milliseconds before the start of a head sweep, suggesting that it may be part of an active preparatory behaviour. Similar preparatory behaviours have been observed in caterpillars before cantilevering behaviours (Lin et al., 2011), adult flies during fast escape behaviours (Card & Dickinson, 2008) and humans during stepping (Watanabe & Higuchi, 2022).

We also observed transient tripod-shaped substrate interactions in posterior terminal regions of larvae immediately before forward waves and headsweeps. Two bilateral cuticular protrusions covered in trichomes, labelled in previous work as anal papillae (Zanini et al., 2016), are likely candidates responsible for these substrate interactions. The actions of these structures have not previously been described as a part of movement in soft-bodied animals. What is the function of this transient tripod? Each body segment has a preceding substrate-planted segment which acts as the anchor and lever to push the animal forward. However, A8 is an exception; it has no full preceding segment in contact with the substrate to counteract its muscle contraction. The tripod processes are ideally positioned to provide an anchor against horizontal reaction force generated by A8

when moving forward (**Figure 7A**), and might effectively form a temporary extra segment prior to initiation of a wave (**Figure 7B**). The deployment of cuticular features as transient anchors has not been a focus of previous studies; future work could incorporate our finding into models of crawling behaviour.

Evidence for functional subdivisions within protopodia

By examining the dynamics of individual footfalls, we found that protopodia exhibited characteristic spatiotemporal force patterns across the footfall cycle. This shows parallels to the regional specificity of function in a vertebrate foot. Specifically, the posterior medial region of the protopodia makes a large contribution to peak GRFs exerted during ST (**Figure 7B**), similar in nature to a vertebrate heel strike impacting the surface prior to the rest of the foot. We propose that this zone of the protopodia acts as a vaulting point, functioning as a 'point d'appui' (point of support) as proposed in other soft-bodied animals (Trueman, 1975; Valentine, 1989). The transience of this vaulting point suggests it may be critical for locomotion, but dispensable for postural control during StP. The distal area of protopodia exhibited a similar transience. Immediately after the posterior and medial protopodia impact during ST, the contact area of the outer region of the protopodia grew across both the AP and the ML axes. However, throughout the StP, this outer region then slowly retracted, suggesting it too was not critically important for maintaining posture during StP. This may reflect a transient anchoring mechanism – specifically, this anchor region deploys to provide greater friction for the subsequent segments (**Figure 7C**). This would allow the contractile wave to progress unimpeded by reaction forces produced according to Newton's 3rd law. Previously, such a function was thought to be provided mainly by mucoid adhesion (Trueman, 1975). However, *Drosophila* larvae are proficient at crawling over wet surfaces where mucoid adhesion is reduced or impossible (Apostolopoulou et al., 2014). Larvae can adhere to dry surfaces but have difficulty moving over these, although mucoid adhesion would provide optimal anchorage in this context. We propose that protopodia act to provide an optimal balance between anchorage and adhesion depending on the environmental context. Overall, this suggests that *Drosophila* larvae use a sophisticated process of articulating, positioning and sequestering protopodia to enable movement over terrain. Future work will be needed to

determine the extent to which these processes are conserved across other soft-bodied crawlers.

Conclusions and outlook for future work

Combining ERISM-WARP with a genetically tractable model organism opens new avenues for understanding the biomechanical basis of animal behaviour, as well as the operation of miniaturized machines. Here we used *Drosophila* larvae as a test case, but our methods now allow elastic optical resonators to be tuned to a wide range of animal sizes and thus create new possibilities for studying principles of neuro-biomechanics across an array of animals. In parallel, roboticists are increasingly moving to create miniaturized soft robots for a variety of applications. Our approach is well suited to provide ground truth, constraints, and inspiration for the development of such miniaturized machines. It also provides a potentially powerful new resource for evaluating the performance of these devices, as our methodology will also allow scientists to measure GRFs during the operation of miniaturized soft machines. Importantly, while we have focused here on the movement of soft animals, our sensors could also be tuned to measure forces produced by small limbed animals or miniaturized machines with rigid internal or external skeletons. Overall, this work therefore establishes a flexible platform for future investigations aimed at integrating knowledge across genetics, neuroethology, biomechanics, and robotics.

Methods

Animal Rearing

Animals were raised on standard cornmeal and yeast medium (17.4 g/L yeast, 73.1 g/L cornmeal, 5.8 g/L agar, 4.8 ml/L propionate) at 25°C with a 12-hour light-dark cycle except where explicitly stated otherwise. Animals were given at least 1 hour to acclimate to room temperature prior to all experiments. Immediately prior to experiments, samples of media containing larvae were taken using a spatula before being placed into a columnar stacked sieve with 40, 60 and 100 meshes from top to bottom, respectively. Media samples were run under gentle flowing tap water to separate adult debris, 2nd instar larvae and 1st instar larvae with embryos on each mesh. Larvae from the 60-mesh fraction of the sieve were observed under a microscope and animals around 1 mm were selected and washed before being placed on 1% (w/v) agarose lined dishes.

Denticle band kinematic imaging

All animals were raised in ambient light conditions at room temperature. Between 48 and 72 hours after flies were introduced to fresh media, feeding 2nd instar Canton-S wildtype animals were selected with a size exclusion criterion - any animals below 0.8 mm or above 1.5 mm were rejected. Animals were then washed and allowed to acclimate to 0.5% (w/v) agarose.

Immediately before experiments, a single animal was transferred to a freshly set dish containing 0.5% (w/v) agarose while still transparent. These dishes were then quickly placed onto the 3D printed stage of a custom-built inverted Bresser Advance ICD stereomicroscope (Bresser GmbH, Rhede, Germany). Denticle band images were acquired, through the still transparent agarose substrate, at 60 frames per second for at least 1 minute while the larva was freely behaving. All images were acquired using a XIMEA CMOS camera (XIMEA GmBH, Münster, Germany) through MicroManager 1.4 (Edelstein et al., 2014). The velocity of 33 individual identifiable points across the animal's body during peristaltic waves whilst imaging from the ventral side of 2nd instar larvae Denticle bands were tracked manually using the Manual Tracking plugin of ImageJ (Schindelin et al., 2012). Analysis of tracking data was performed using OriginPro 2019 (OriginLab Corporation, MA, USA).

ERISM and WARP imaging

Elastic Resonator Interference Stress microscopy (ERISM) was used to record high-resolution maps of substrate indentations by monitoring local changes in the resonances of a soft and deformable optical microcavity. ERISM has been used to quantify cellular forces down to the piconewton range. The static thickness of microcavities was measured adapting our previously published ERISM method as described in (Kronenberg et al., 2017a; Liehm et al., 2018). In brief, images of the cavity were taken under epi-illumination with a series of 201 different wavelengths (550-750nm in 1nm steps). From these images, the minima in the spectral reflection for each pixel were correlated with theoretical values obtained from optical modelling for cavities of different thicknesses to determine the actual thickness at each position across the image. (Cavities were between 8-12µm in static thickness.) Thickness maps were converted into maps of local displacement by subtracting a linear plane, using the mean thickness of the cavity in each corner.

For dynamic force mapping, we used a further improved version of the WARP routine described in (Meek et al., 2021). Epi-illumination with light of two different and quickly alternating wavelengths was produced by passing the emission from two identical red LEDs (dominant emission wavelength 625nm, FWHM 17nm; Thorlabs Inc. NJ, USA) through two identical narrow bandpass filters (peak transmission at 633nm, FWHM of 1nm; Thorlabs Inc., NJ, USA). By tilting the filter located in front of one of the LEDs by approximately 15 degrees relative to the incident light, its peak transmission wavelength was tuned to λ_θ=628nm. For the optical modes supported by our microcavities, this corresponds to a phase shift of roughly 90°, but remains within the same free spectral range band of the cavity. For the WARP measurements, we first took calibration images (under subsequent illumination at λ and λ_θ) of the empty microcavity in an area with roughly linear slope in cavity thickness, e.g. near where the silicone well containing the larvae meets the surface of the cavity. Images of behaving larvae were then recorded under rapidly alternating illumination at λ and λ_θ, with the camera sending alternating trigger pulses to each LED to generate interleaved stacks of λ and λ_θ images.

Displacement maps were obtained from these stacks using a series of image transformations, based around the fact that the ratio of the difference and the sum of pixel

intensities at λ and λ_θ is linked to local thickness in an unambiguous manner, at least across each free spectral range. See Supporting Information Fig. S4 and (Meek et al., 2021) for further details on the calculation of displacement from the λ and λ_θ images. All WARP and ERISM images were acquired using an Andor Zyla 4.2 sCMOS camera (Andor Technology, Belfast, UK).

Stress maps were calculated from the ERISM and WARP displacement maps as described previously (Kronenberg et al., 2017a), using a finite element method simulation via COMSOL multiphysics (COMSOL Ltd., Cambridge, UK) and the known mechanical properties of the microcavity.

Polydimethylsiloxane gel preparation

Polydimethylsiloxane elastomers were prepared according to manufacturer guidelines for all gels. The two component precursors of different gels were mixed together in separate glass bottles, using an equal mass ratio of the two components for Sylgard 527 and NulSil Gel8100 but a 1:10 volumetric ratio for Sylgard 184. Mixing was performed by 10 min of magnetic stirring (Sylgard 527 and NuSil GEL8100) or by 10 min of mechanical stirring (Sylgard 184). The elastomer mixtures were then combined in a fresh bottle in the desired mass ratio using a syringe following the same method as (Palchesko et al., 2012). Combined elastomers were mixed for a further 10 minutes. Mixtures containing Sylgard®184 were initially mixed by high speed vortexing to coarsely disperse the gel to allow for the magnetic stir bar to overcome the high viscosity of the gel. After mixing, all preparations were degassed under vacuum for around 5 minutes, prior to fabrication of microcavities.

Microcavity fabrication

The fabrication protocol of elastic microcavities was adapted from (Kronenberg et al., 2017b). 24 mm^2 borosilicate glass substrates of No.5 thickness were cleaned via ultrasonication in acetone followed by propan-2-ol for 3 minutes. After cleaning, substrates were dried using N_2 and baked at 125°C for 10 minutes to clear any residual solvent. Cleaned glass substrates were then plasma treated with oxygen plasma for 3 minutes at 20 SCCM O_2 flow rate to clear any residual organics and activate the surface of the glass. Cleaned and activated glass substrates were then sputter coated with 0.5nm

of Cr, which acted as an adhesion layer for the subsequent 10nm Au layer which was deposited by thermal vapour deposition. 50nm of SiO_2 was then deposited by sputter coating to improve stability of the resultant bottom mirrors. Roughly 100µl of pre-mixed and degassed polydimethylsiloxane gels was spincoated onto the bottom mirrors at 3000RPM, 1500RPM acceleration, for 60 seconds and then quickly transferred to a pre-heated metal plate at 150°C for 1.5 hr to cure the elastomer. After curing, elastomer coated bottom mirrors were O_2 plasma treated with the desired plasma power at 20 SCCM O_2 flow rate for 10 seconds. 15nm of Au was then deposited onto the oxidised elastomer, thus completing the microcavity.

Microcavity characterisation

Microcavities were characterised using a NanoSurf Flex Atomic Force Microscope (Nanosurf, Liestal, Switzerland). 15-18µm diameter glass beads were glued to the tip of Uniqprobe™ QPCont cantilevers (Nanosensors AG, Neuchatel, Switzerland) using a UV-polymer glue after thermal calibration of the spring constant at 21°C. Sphere-tipped cantilevers were then indented into microcavity samples at 1µm/s with up to 30nN of force. This process was repeated across the surface of the microcavity at least 5 times, with each measurement being roughly 2mm apart to get a measure of the variation across the cavity surface. Force-distance profiles recorded by the AFM were then fitted to the Hertz model to compute the Young's modulus at each point of each sample. Mean cavity lengths were measured by taking 4 ERISM images at 4x magnification from each corner of the cavity, and then taking the mean of 4 regions of interest per image.

Prior to use in experiments, a low pH Collagen-I (1mg/ml; Millipore L7220) solution was prepared at a 1:1 (v/v) ratio with pH3 phosphate buffered saline (PBS). pH3 PBS was prepared with either hydrochloric acid or acetic acid, mixing until pH3 was recorded using an electronic pH meter. Collagen-I mixtures were then dosed onto microcavities in silicone wells (1ml per microcavity) and allowed to coat the surface overnight at 4°C. Immediately before the experiment, microcavities were washed with deionised water at least 5 times, taking care not to remove all liquid to prevent damage to the top gold surface.

Anaesthetised animal force imaging

Animals were selected, cleaned, and placed in a fridge at 4°C for 2-3 hours to anaesthetise them. Immediately prior to experiments, anaesthetised animals were gently placed onto a collagen coated microcavity in a petri-dish on ice. The microcavities were then placed on the ERISM-WARP microscope and the animals were observed carefully. As soon as mouth-hook movement was observed, an ERISM measurement was taken. Animals often had to be placed back onto ice to anaesthetise them once more as they rapidly regained motility. As the complete ERISM scan requires ca. 5 seconds, animals were required to be completely stationary in order to get reliable stress map images.

Freely behaving animals force imaging

Animals were selected according to the previously outlined criteria and cleaned before being placed onto a 1% (w/v) agarose lined petri dish. Elastic resonators were prepared according to the coating criteria mentioned above. 10% Nusil®GEL8100, 180W O_2 plasma treated microcavities were used for all freely behaving experiments. Once calibration images of the microcavity were acquired, excess water was removed from the cavity and animals were gently placed onto the cavity surface with a paintbrush, taking care to ensure there was enough moisture on the animal to prevent drying. In order to keep animals on the sensor surface, a 50µl drop of 15mM ethyl butanoate (Sigma-Aldrich Inc., MO, USA), suspended in paraffin oil, was dropped onto a 24 mm^2 glass coverslip before being inverted and placed on top of the silicone well (ibidi GmbH, Munich, Germany) such that the attractive odorant faced towards the animal but perpetually out of its reach. Animals were then imaged by WARP and displacement and stress maps were generated as described above.

Statistical Analyses

All statistical analysis was performed using OriginPro 2019 (OriginLab Corporation, MA, USA). Coefficients of determination (R^2) for all but displaced volume vs contact area analysis were determined using a linear fit. The rarity of backwards waves during normal larval behaviour precluded analysis of latencies as used in **Figure 2**. Coefficients of determination for the displaced volume vs contact area analysis was performed using a 2nd order polynomial fit instead as this describes the data better than a linear fit. Two-

way repeated measures ANOVA was used in segmentwise peak contact area analysis, as data were normally distributed according to a Shapiro-Wilk test. However, Levene's test for homogeneity of variances was significant for SI ($p<0.05$) but not for ST ($p=0.092$), we urge caution when interpreting the within-subjects' effects. Mauchly's test showed sphericity of segment ($W=0.082$, $p=0.063$) and the segment*SI-ST interaction ($W=0.27428$, $p=0.62463$), where the SI-ST factor was not tested due to insufficient degrees of freedom. Independent samples t-test was performed to show no significant difference between larval behaviour on elastic resonators and standard agarose substrates as data were normally distributed according to a Shapiro-Wilk test. Pairwise comparisons between segments all used Tukey-corrected t-tests. Force-distance curves were fitted using a height-corrected Hertz Model; all force-distance curves were fitted with an $R^2>0.9$.

Acknowledgements

This work was supported by EPSRC (Doctoral Training grant EP/L505079/1 and grant EP/P030017/1), the European Research Council under the European Union's Horizon 2020 Framework Programme (FP/2014-202) ERC grant agreement no. 640012 (ABLASE), and the Alexander von Humboldt Foundation via the Humboldt Professorship to MCG. We thank our technicians Audrey Grant and Tanya Sneddon for preparing fly food, Dr Eleni Dalaka for her support during atomic force microscopy experiments, Dr Andreas Mischok for his advice with fabrication, Dr Marcus Bischoff for his advice and support early in the work, and Dr Jacob Francis and Dr James MacLeod for their methodological advice regarding lateral view imaging.

Author Contributions

Experiments were conceived and designed by J.H.B., M.C.G. and S.R.P.; fabrication and experiments were performed by J.H.B., method was designed by N.M.K. and A.M.; data analysis was performed by J.H.B., N.M.K. and A.M.; animal rearing was performed by J.H.B. and S.R.P; writing was performed by J.H.B. and S.R.P. with input from by M.C.G., N.M.K. and A.M.

References

Ahearne, M., Yang, Y., el Haj, A. J., Then, K. Y., & Liu, K.-K. (2005). Characterizing the viscoelastic properties of thin hydrogel-based constructs for tissue engineering applications. *Journal of the Royal Society, Interface*, *2*(5), 455–463. https://doi.org/10.1098/rsif.2005.0065

Apostolopoulou, A., Hersperger, F., Mazija, L., Widmann, A., Wüst, A., & Thum, A. (2014). Composition of agarose substrate affects behavioral output of *Drosophila* larvae. *Frontiers in Behavioral Neuroscience*, *8*, 11. https://doi.org/10.3389/fnbeh.2014.00011

Audu, M. L., Kirsch, R. F., & Triolo, R. J. (2007). Experimental verification of a computational technique for determining ground reactions in human bipedal stance. *Journal of Biomechanics*, *40*(5), 1115–1124. https://doi.org/10.1016/j.jbiomech.2006.04.016

Berrigan, D., & Pepin, D. J. (1995). How maggots move: Allometry and kinematics of crawling in larval Diptera. *Journal of Insect Physiology*, *41*(4), 329–337. https://doi.org/10.1016/0022-1910(94)00113-U

Bobbert, M., Gomez Alvarez, C., van Weeren, R., Roepstorff, L., & Weishaupt, M. (2007). A new method to calculate peak vertical ground reaction forces on individual limbs from kinematics of trotting horses. *Comparative Biochemistry and Physiology A – Molecular & Integrative Physiology*, *146*(4), S110–S110.

Budd, G. E. (2001). Why are arthropods segmented? *Evolution and Development*, *3*(5), 332–342. https://doi.org/10.1046/J.1525-142X.2001.01041.X

Burnette, D. T., Shao, L., Ott, C., Pasapera, A. M., Fischer, R. S., Baird, M. A., der Loughian, C., Delanoe-Ayari, H., Paszek, M. J., Davidson, M. W., Betzig, E., & Lippincott-Schwartz, J. (2014). A contractile and counterbalancing adhesion system controls the 3D shape of crawling cells. *Journal of Cell Biology, 205(1), 83–96*. https://doi.org/10.1083/jcb.201311104

Cacciatore, T. W., Rozenshteyn, R., & Kristan, W. B. (2000). Kinematics and Modeling of Leech Crawling: Evidence for an Oscillatory Behavior Produced by Propagating Waves of Excitation. *Journal of Neuroscience*, *20*(4), 1643–1655. https://doi.org/10.1523/JNEUROSCI.20-04-01643.2000

Card, G., & Dickinson, M. H. (2008). Visually Mediated Motor Planning in the Escape Response of *Drosophila*. *Current Biology*, *18*(17), 1300–1307. https://doi.org/https://doi.org/10.1016/j.cub.2008.07.094

Clark, M. Q., Zarin, A. A., Carreira-Rosario, A., & Doe, C. Q. (2018). Neural circuits driving larval locomotion in *Drosophila*. *Neural Development*, *13*(1), 6. https://doi.org/10.1186/s13064-018-0103-z

Dalaka, E., Kronenberg, N. M., Liehm, P., Segall, J. E., Prystowsky, M. B., & Gather, M. C. (2020). Direct measurement of vertical forces shows correlation between mechanical activity and proteolytic ability of invadopodia. *Science Advances*, *6*(11), eaax6912. https://doi.org/10.1126/sciadv.aax6912

Dimitriadis, E. K., Horkay, F., Maresca, J., Kachar, B., & Chadwick, R. S. (2002). Determination of Elastic Moduli of Thin Layers of Soft Material Using the Atomic Force Microscope. *Biophysical Journal*, *82*(5), 2798–2810. https://doi.org/10.1016/S0006-3495(02)75620-8

Edelstein, A. D., Tsuchida, M. A., Amodaj, N., Pinkard, H., Vale, R. D., & Stuurman, N. (2014). Advanced methods of microscope control using μManager software. *Journal of Biological Methods*, *1*(2). https://doi.org/10.14440/jbm.2014.36

Fang-Yen, C., Wyart, M., Xie, J., Kawai, R., Kodger, T., Chen, S., Wen, Q., & Samuel, A. D. T. (2010). Biomechanical analysis of gait adaptation in the nematode *Caenorhabditis elegans*. *Proceedings of the National Academy of Sciences*, *107*(47), 20323–20328. https://doi.org/10.1073/pnas.1003016107

Federle, W., & Labonte, D. (2019). Dynamic biological adhesion: mechanisms for controlling attachment during locomotion. *Philosophical Transactions of the Royal Society of London. Series B, Biological Sciences*, *374*(1784), 20190199. https://doi.org/10.1098/rstb.2019.0199

Fitzpatrick, M. J., & Szewczyk, E. (2005). Locomotion is not influenced by denticle number in larvae of the fruit fly *Drosophila melanogaster*. *Canadian Journal of Zoology*, *83*(2), 368–371. https://doi.org/10.1139/z05-027

Friesen, K., Chen, H., Zhu, J., & Taylor, D. B. (2015). External Morphology of Stable Fly (Diptera: *Muscidae*) Larvae. *Journal of Medical Entomology*, *52*(4), 626–637. https://doi.org/10.1093/jme/tjv052

Fushiki, A., Zwart, M. F., Kohsaka, H., Fetter, R. D., Cardona, A., & Nose, A. (2016). A circuit mechanism for the propagation of waves of muscle contraction in *Drosophila*. *ELife*, *5*, e13253. https://doi.org/10.7554/eLife.13253

Gjorgjieva, J., Biron, D., & Haspel, G. (2014). Neurobiology of *Caenorhabditis elegans* Locomotion: Where Do We Stand? *BioScience*, *64*(6), 476–486. https://doi.org/10.1093/biosci/biu058

Gray, J., & Lissmann, H. W. (1964). The Locomotion of Nematodes. *Journal of Experimental Biology*, *41*(1), 135–154. https://doi.org/10.1242/JEB.41.1.135

Heckscher, E. S., Lockery, S. R., & Doe, C. Q. (2012). Characterization of Drosophila Larval Crawling at the Level of Organism, Segment, and Somatic Body Wall Musculature. *Journal of Neuroscience*, *32*(36), 12460–12471. https://doi.org/10.1523/JNEUROSCI.0222-12.2012

Kampowski, T., Eberhard, L., Gallenmüller, F., Speck, T., & Poppinga, S. (2016). Functional morphology of suction discs and attachment performance of the Mediterranean medicinal leech (*Hirudo verbana Carena*). *Journal of The Royal Society Interface*, *13*(117), 20160096. https://doi.org/10.1098/rsif.2016.0096

Khare, S. M., Awasthi, A., Venkataraman, V., & Koushika, S. P. (2015). Colored polydimethylsiloxane micropillar arrays for high throughput measurements of forces applied by genetic model organisms. *Biomicrofluidics*, *9*(1), 14111. https://doi.org/10.1063/1.4906905

Kim, S., Laschi, C., & Trimmer, B. (2013). Soft robotics: a bioinspired evolution in robotics. *Trends in Biotechnology*, *31*(5), 287–294. https://doi.org/10.1016/j.tibtech.2013.03.002

Kronenberg, N. M., Liehm, P., & Gather, M. C. (2017b). Fabrication of elastic micro-cavity chips for use in Elastic Resonator Interference Stress Microscopy. *Protocol Exchange*. https://doi.org/10.1038/protex.2017.052

Kronenberg, N. M., Liehm, P., Steude, A., Knipper, J. A., Borger, J. G., Scarcelli, G., Franze, K., Powis, S. J., & Gather, M. C. (2017a). Long-term imaging of cellular forces with high precision by elastic resonator interference stress microscopy. *Nature Cell Biology, 19*, 864–872. https://doi.org/10.1038/ncb3561

Liehm, P., Kronenberg, N. M., & Gather, M. C. (2018). Analysis of the Precision, Robustness, and Speed of Elastic Resonator Interference Stress Microscopy. *Biophysical Journal 114*(9), 2180–2193. https://doi.org/10.1016/j.bpj.2018.03.034

Lin, H. T., & Trimmer, B. A. (2010). The substrate as a skeleton: ground reaction forces from a soft-bodied legged animal. *Journal of Experimental Biology*, *213*(7), 1133–1142. https://doi.org/10.1242/jeb.037796

Lin, H.-T., Slate, D. J., Paetsch, C. R., Dorfmann, A. L., & Trimmer, B. A. (2011). Scaling of caterpillar body properties and its biomechanical implications for the use of a hydrostatic skeleton. *Journal of Experimental Biology*, *214*(7), 1194–1204. https://doi.org/10.1242/jeb.051029

Lin, H.-T., & Trimmer, B. A. (2012). A new bi-axial cantilever beam design for biomechanics force measurements. *Journal of Biomechanics*, *45*(13), 2310–2314. https://doi.org/10.1016/j.jbiomech.2012.06.005

Loveless, J., Garner, A., Issa, A. R., Webb, B., Ohyama, T., & Alonso, C. R. (2020). A physical theory of larval *Drosophila* behaviour. *BioRxiv*. https://doi.org/10.1101/2020.08.25.266163

Loveless, J., Lagogiannis, K., & Webb, B. (2019). Modelling the mechanics of exploration in larval *Drosophila*. *PLOS Computational Biology*, *15*(7), 1–33. https://doi.org/10.1371/journal.pcbi.1006635

Lu, H., Zhang, M., Yang, Y., Huang, Q., Fukuda, T., Wang, Z., & Shen, Y. (2018). A bioinspired multilegged soft millirobot that functions in both dry and wet conditions. *Nature Communications*, *9*(1), 3944. https://doi.org/10.1038/s41467-018-06491-9

Mantziaris, C., Bockemühl, T., & Büschges, A. (2020). Central pattern generating networks in insect locomotion. *Developmental Neurobiology*, *80*(1–2), 16–30. https://doi.org/10.1002/dneu.22738

Meek, A. T., Kronenberg, N. M., Morton, A., Liehm, P., Murawski, J., Dalaka, E., Booth, J. H., Powis, S. J., & Gather, M. C. (2021). Real-time imaging of cellular forces using optical interference. *Nature Communications*, *12*(1), 3552. https://doi.org/10.1038/s41467-021-23734-4

Mohammed, D., Versaevel, M., Bruyère, C., Alaimo, L., Luciano, M., Vercruysse, E., Procès, A., & Gabriele, S. (2019). Innovative tools for mechanobiology: Unraveling outside-in and inside-out mechanotransduction. In *Frontiers in Bioengineering and Biotechnology*. https://doi.org/10.3389/fbioe.2019.00162

Ormerod, K. G., Scibelli, A. E., & Littleton, J. T. (2022). Regulation of excitation-contraction coupling at the *Drosophila* neuromuscular junction. *The Journal of Physiology*, *600*(2), 349–372. https://doi.org/10.1113/JP282092

Palchesko, R. N., Zhang, L., Sun, Y., & Feinberg, A. W. (2012). Development of Polydimethylsiloxane Substrates with Tunable Elastic Modulus to Study Cell Mechanobiology in Muscle and Nerve. *PLOS ONE*, *7*(12), e51499. https://doi.org/10.1371/journal.pone.0051499

Payre, F. (2004). Genetic control of epidermis differentiation in *Drosophila*. *The International Journal of Developmental Biology*, *48*(2–3), 207–215. https://doi.org/10.1387/ijdb.15272387

Pritchard, R. H., Lava, P., Debruyne, D., & Terentjev, E. M. (2013). Precise determination of the Poisson ratio in soft materials with 2D digital image correlation. *Soft Matter*, *9*(26), 6037–6045. https://doi.org/10.1039/C3SM50901J

Pulver, S. R., Bayley, T. G., Taylor, A. L., Berni, J., Bate, M., & Hedwig, B. (2015). Imaging fictive locomotor patterns in larval *Drosophila*. *Journal of Neurophysiology*, *114*(5), 2564–2577. https://doi.org/10.1152/jn.00731.2015

Salerno, M., Dante, S., Patra, N., & Diaspro, A. (2010). AFM measurement of the stiffness of layers of agarose gel patterned with polylysine. *Microscopy Research and Technique*, *73*(10), 982–990. https://doi.org/10.1002/jemt.20838

Schindelin, J., Arganda-Carreras, I., Frise, E., Kaynig, V., Longair, M., Pietzsch, T., Preibisch, S., Rueden, C., Saalfeld, S., Schmid, B., Tinevez, J.-Y., White, D. J., Hartenstein, V., Eliceiri, K., Tomancak, P., & Cardona, A. (2012). Fiji: an open-source platform for biological-image analysis. *Nature Methods*, *9*(7), 676–682. https://doi.org/10.1038/nmeth.2019

Schneider-Mizell, C. M., Gerhard, S., Longair, M., Kazimiers, T., Li, F., Zwart, M. F., Champion, A., Midgley, F. M., Fetter, R. D., Saalfeld, S., & Cardona, A. (2016). Quantitative neuroanatomy for connectomics in *Drosophila*. *ELife*, *5*, e12059. https://doi.org/10.7554/eLife.12059

Simon, M. A., Fusillo, S. J., Colman, K., & Trimmer, B. A. (2010). Motor patterns associated with crawling in a soft-bodied arthropod. *Journal of Experimental Biology*, *213*(13), 2303–2309. https://doi.org/10.1242/jeb.039206

Sun, X., Liu, Y., Liu, C., Mayumi, K., Ito, K., Nose, A., & Kohsaka, H. (2022). A neuromechanical model for *Drosophila* larval crawling based on physical measurements. *BMC Biology*, *20*(1), 130. https://doi.org/10.1186/s12915-022-01336-w

Tanaka, Y., Ito, K., Nakagaki, T., & Kobayashi, R. (2012). Mechanics of peristaltic locomotion and role of anchoring. *Journal of the Royal Society, Interface*, *9*(67), 222–233. https://doi.org/10.1098/rsif.2011.0339

Trueman, E. R. (1975). *The Locomotion of Soft-Bodied Animals*. Edward Arnold.

Tytell, E. D., Holmes, P., & Cohen, A. H. (2011). Spikes alone do not behavior make: why neuroscience needs biomechanics. *Current Opinion in Neurobiology*, *21*(5), 816–822. https://doi.org/10.1016/j.conb.2011.05.017

Vaadia, R. D., Li, W., Voleti, V., Singhania, A., Hillman, E. M. C., & Grueber, W. B. (2019). Characterization of Proprioceptive System Dynamics in Behaving *Drosophila* Larvae Using High-Speed Volumetric Microscopy. *Current Biology*, *29*(6), 935-944.e4. https://doi.org/10.1016/j.cub.2019.01.060

Valentine, J. W. (1989). Bilaterians of the Precambrian-Cambrian transition and the annelid-arthropod relationship. *Proceedings of the National Academy of Sciences*, *86*(7), 2272–2275. https://doi.org/10.1073/pnas.86.7.2272

van Griethuijsen, L. I., & Trimmer, B. A. (2014). Locomotion in caterpillars. *Biological Reviews*, *89*(3), 656–670. https://doi.org/10.1111/brv.12073

Watanabe, R., & Higuchi, T. (2022). Anticipatory action planning for stepping onto competing potential targets. *Frontiers in Human Neuroscience*, *16*. https://doi.org/10.3389/fnhum.2022.875249

Zanini, R., Deprá, M., & Valente, V. (2016). Ultrastructural characterization of the pre-adult stages of *Drosophila willistoni* species group (Diptera, *Drosophilidae*). *Trends in Entomology*, *12*, 43–50.

Zhang, H., Gonzalez-Gomez, J., & Zhang, J. (2009). A new application of modular robots on analysis of caterpillar-like locomotion. *2009 IEEE International Conference on Mechatronics*, 1–6. https://doi.org/10.1109/ICMECH.2009.4957149

Zwart, M. F., Pulver, S. R., Truman, J. W., Fushiki, A., Fetter, R. D., Cardona, A., & Landgraf, M. (2016). Selective Inhibition Mediates the Sequential Recruitment of Motor Pools. *Neuron*, *91*(3), 615–628. https://doi.org/10.1016/j.neuron.2016.06.031

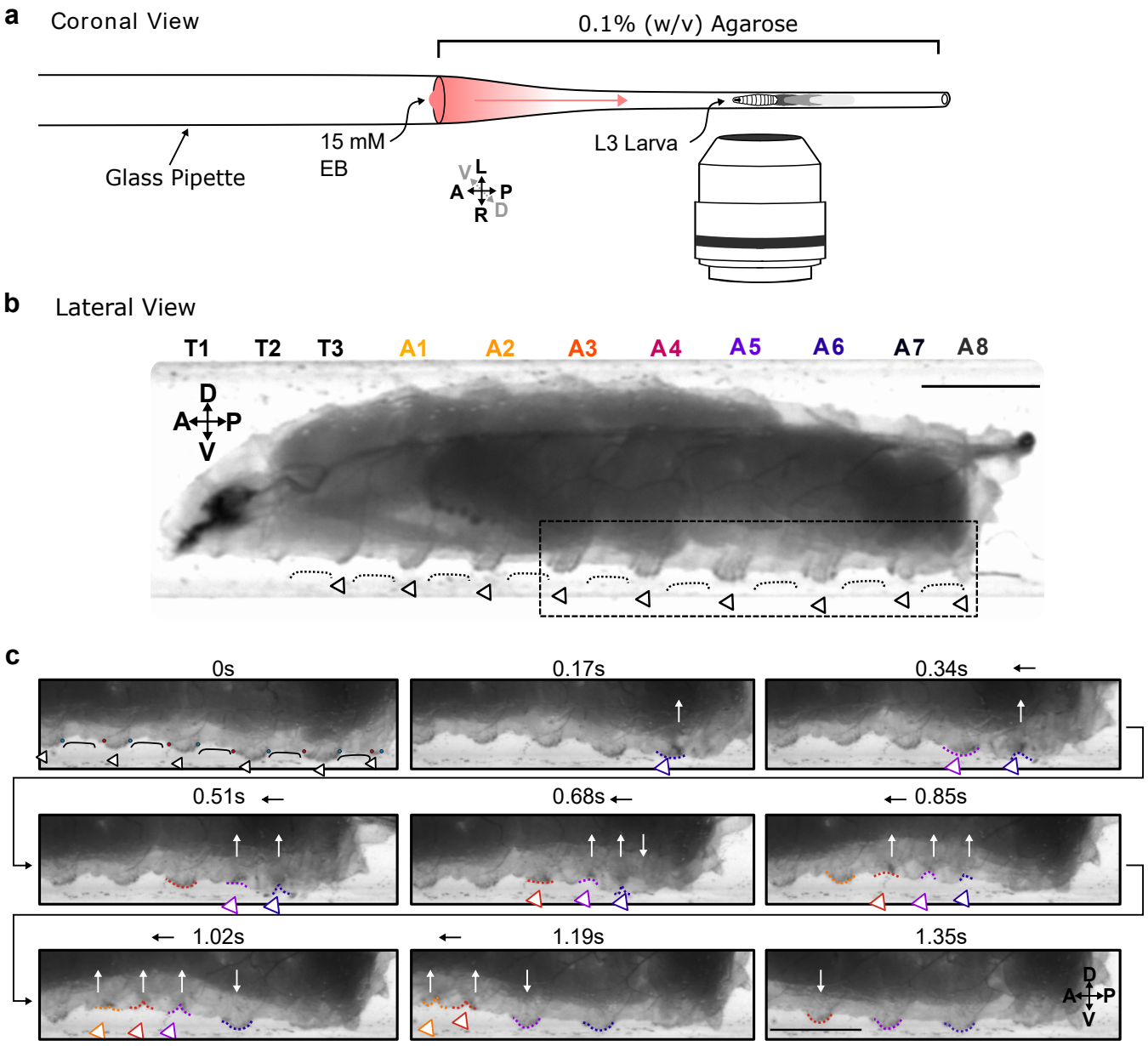
a
Coronal View
0.1% (w/v) Agarose
Glass Pipette
15 mM
EB
L3 Larva
V L
A P
R D
b
Lateral View
T1 T2 T3 A1 A2 A3 A4 A5 A6 A7 A8
D
A P
V
c
0s
0.17s
0.34s
0.51s
0.68s
0.85s
1.02s
1.19s
1.35s
D
A P
V

Figure 1. Protopodia protrusions in each segment are sequestered during swing phases of forwards locomotion.

a, Schematic of setup for lateral imaging of larvae, using confinement in Pasteur pipette pre-filled with 0.1% (w/v) agarose. To encourage forward crawling, 10µl of 15mM ethyl butanoate (EB) was placed as attractive odour at the end of the pipette. **b**, Lateral brightfield image of 3rd instar larva showing convex areas of denticle bands (open arrowheads) protruding into the substrate, interdigitated by concave areas of naked cuticle (black line) not interacting with the substrate. Scale bar=750µm. **c**, Time lapse of area marked by dotted box in **b** showing the swing periods and stance periods of protopodia (coloured open arrowheads and dotted lines) during a forward wave. Red and blue dots at 0s denote anterior and posterior rows of denticles, respectively. As the posterior-most denticle row moved to meet the anterior row of the band, the medial row detached from the substrate via invagination (white arrows). The invaginated pocket is then moved forward (black arrow) and subsequently replanted. This action repeats as the wave propagates. Scale bar=500µm. Images representative of three 3rd instar larvae.

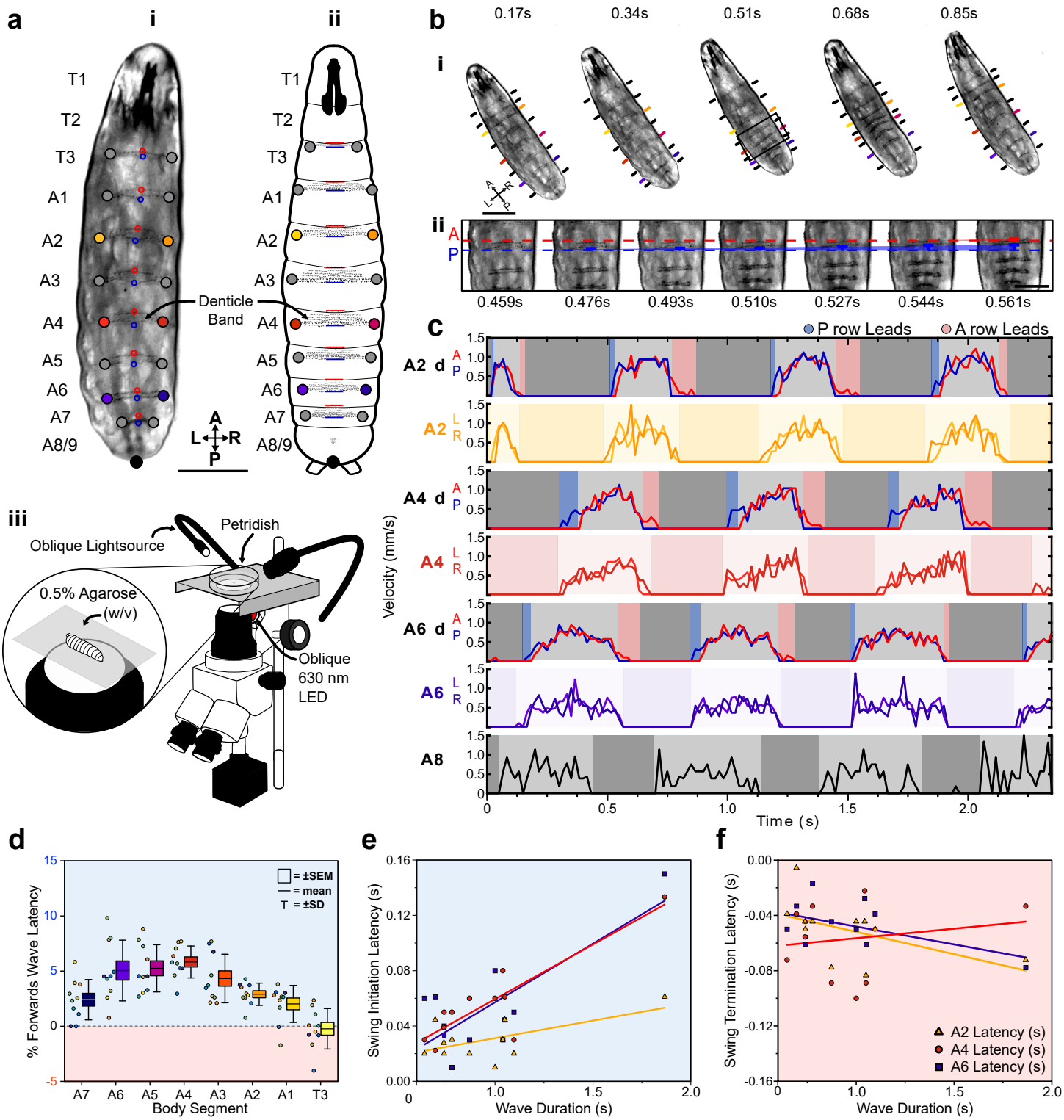
a
i
ii
T1
T2
T3
A1
A2
A3
A4
A5
A6
A7
A8/9
Denticle Band
A
L
R
P
iii
Petridish
Oblique Lightsource
0.5% Agarose (w/v)
Oblique 630 nm LED
b
0.17s
0.34s
0.51s
0.68s
0.85s
0.459s
0.476s
0.493s
0.510s
0.527s
0.544s
0.561s
c
P row Leads
A row Leads
A2 d
A2
A4 d
A4
A6 d
A6
A8
Velocity (mm/s)
Time (s)
d
% Forwards Wave Latency
Body Segment
= ±SEM
= mean
= ±SD
e
Swing Initiation Latency (s)
Wave Duration (s)
f
Swing Termination Latency (s)
Wave Duration (s)
A2 Latency (s)
A4 Latency (s)
A6 Latency (s)

Figure 2. Protopodia kinematics follow 'heel-toe'-like footfall dynamics.

a, (**i**) Brightfield image and (**ii**) schematic of 2nd instar larvae showing ventral side denticle belts which reside upon the protopodia and (**iii**) schematic of the imaging setup used for kinematic tracking. Scale bar=200µm. **b**, (**i**) As a forward wave travels through the animal, the distance between denticle bands decreases. Scale bar=200µm. (**ii**) At higher frame rate and magnification, changes in distance between the posterior and anterior most denticle rows are resolved. The posterior-most row (P, blue) initiates movement first and moves until nearly reaching the anterior-most row (A, red) at 0.544s, after which point, they move together (0.561s). Scale bar=100µm. **c**, Velocity of anterior- and posterior-most denticles rows (A2d A/P, A4d A/P, A6d A/P) and the left/right end of denticle bands (A2 L/R, A4 L/R, A6 L/R and A8 L/R) over three representative forward waves, showing how the strategy observed in **b** is maintained across body segments. Background colours indicate swing initiation (SI, blue), swing period (SwP, light grey), swing termination (ST, pink) and stance period (StP, dark grey). **d**, Forward wave latency for different animals and body segments. Positive values denote posterior row led latency. n=10 animals, 30 waves. **e**, SI-latency is correlated with wave duration in the posterior abdomen (A6: R^2=0.61, purple; A4: R^2=0.78, red) but less so for the anterior abdomen (A2: R^2=0.35, yellow). n=12 animals with 3 latency periods per segment. **f**, ST-latencies show no correlation to wave duration (A6: R^2=0.26, A4: R^2=0.26, A2: R^2=0.03). n=12 animals with 3 latency periods per segment.

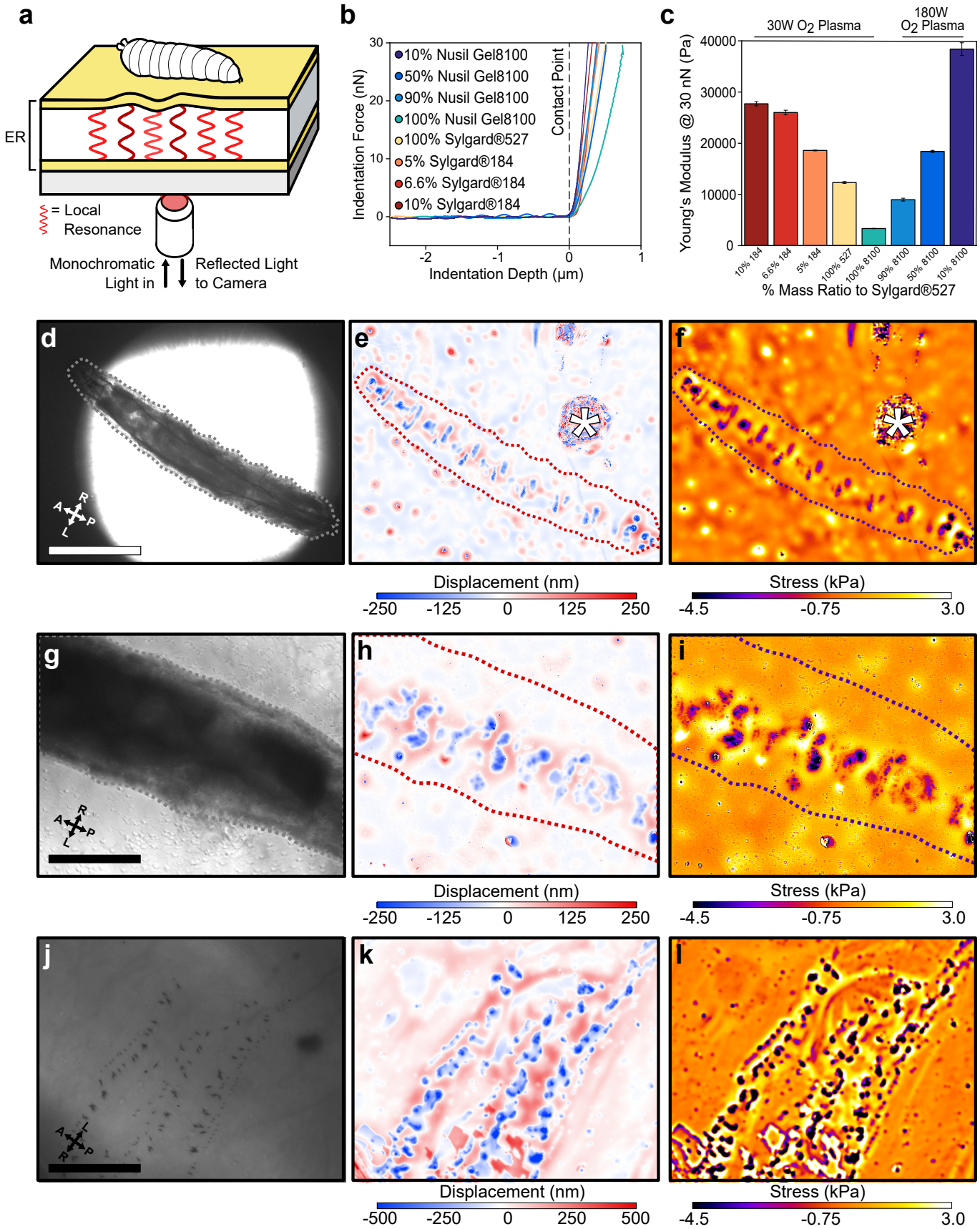
a
ER
= Local Resonance
Monochromatic Light in
Reflected Light to Camera
b
10% Nusil Gel8100
50% Nusil Gel8100
90% Nusil Gel8100
100% Nusil Gel8100
100% Sylgard®527
5% Sylgard®184
6.6% Sylgard®184
10% Sylgard®184
Contact Point
Indentation Force (nN)
Indentation Depth (μm)
c
30W O2 Plasma
180W O2 Plasma
Young's Modulus @ 30 nN (Pa)
% Mass Ratio to Sylgard®527
10% 184
6.6% 184
5% 184
100% 527
100% 8100
90% 8100
50% 8100
10% 8100
d
e
f
Displacement (nm)
Stress (kPa)
g
h
i
j
k
l

Figure 3. ERISM maps mechanical substrate interactions in *Drosophila* larvae. **a**, Schematic of setup for ERISM with *Drosophila* larva on an optical microcavity. Maps of local cavity deformation (displacement) due to indentation forces are generated by analysing cavity resonances. **b**, Force distance relationship measured by AFM and **c**, Mechanical stiffnesses (Young's moduli) for microcavities produced by mixing different elastomers at different ratios and applying different plasma conditions. **d**, **g**, **j**, Brightfield images of anaesthetised 2nd instar larvae recorded at low, medium, and high magnification. **e**, **h**, **k**, Corresponding maps of microcavity displacement. (* denotes contamination on cavity surface from handling the larva.) **f**, **i**, **l**, Corresponding maps of mechanical stress obtained by finite element analysis of displacement maps, showing the stress on the substrate due to passive interaction between larvae and substrate. Scale bar=500µm (**d**), 250µm (**g**) and 50µm (**j**). Images representative of 4 separate 2nd instar larvae. Microcavities in **d**-**i** used 30W O_2 10% Sylgard®184 design, and **j**-**l** used a 30W O_2 5% Sylgard®184 design.

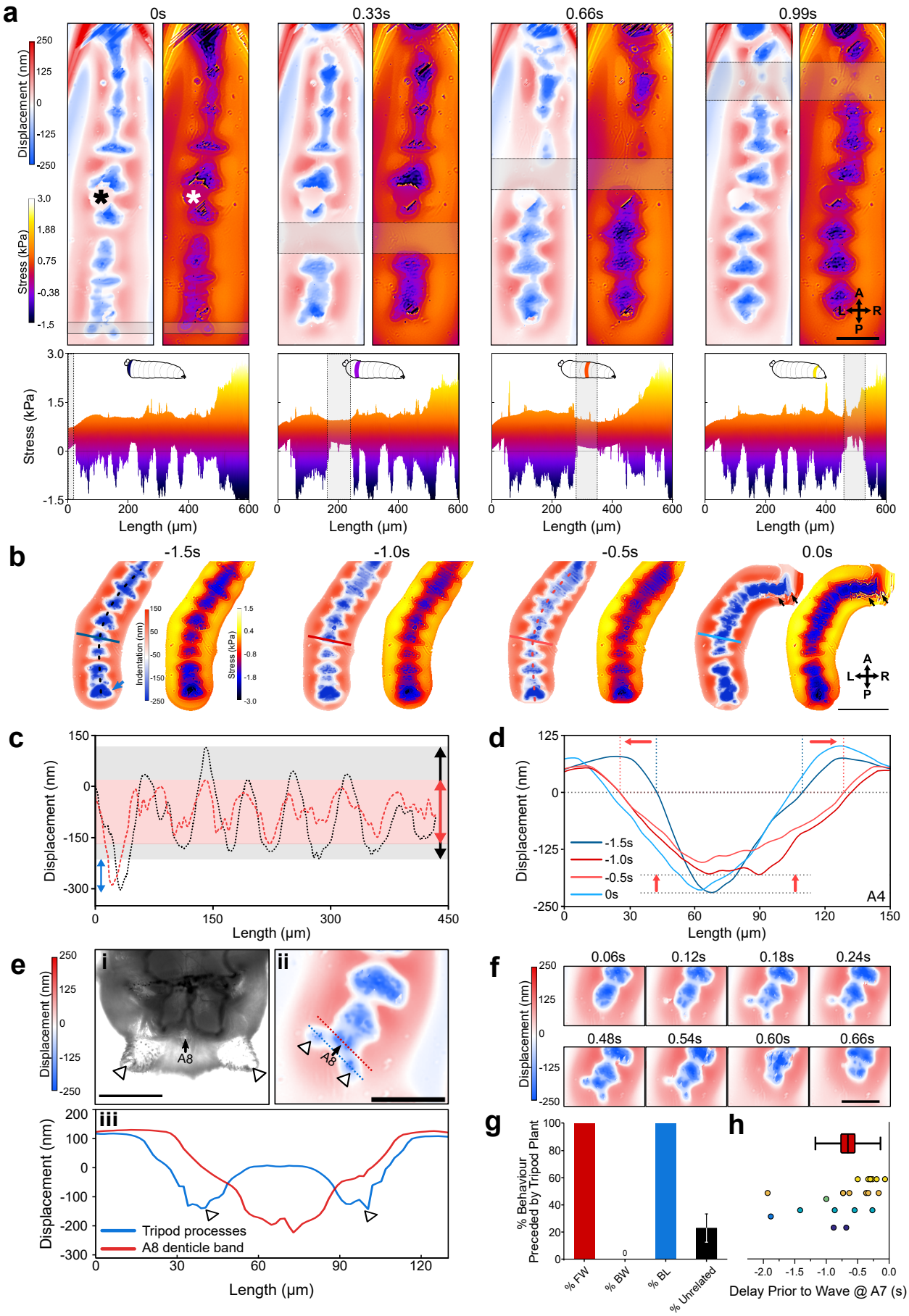
a
0s
0.33s
0.66s
0.99s
Displacement (nm)
Stress (kPa)
Length (µm)
A
L
R
P
b
-1.5s
-1.0s
-0.5s
0.0s
Indentation (nm)
Stress (kPa)
c
Displacement (nm)
Length (µm)
d
Displacement (nm)
Length (µm)
-1.5s
-1.0s
-0.5s
0s
A4
e
i
ii
iii
A8
Displacement (nm)
Length (µm)
Tripod processes
A8 denticle band
f
0.06s
0.12s
0.18s
0.24s
0.48s
0.54s
0.60s
0.66s
Displacement (nm)
g
% Behaviour Preceded by Tripod Plant
% FW
% BW
% BL
% Unrelated
h
Delay Prior to Wave @ A7 (s)

Figure 4. WARP imaging reveals dynamics of substrate interactions during larval movement.

a, WARP image sequence of displacement and stress maps (top) for a freely behaving 2nd instar larva during forward locomotion. (*denotes dust artefact.) Lateral projections of stress maps (bottom) showing individual protopodia interdigitated by naked cuticle. As a contractile wave (grey box) progressed through the animal, protopodia were lifted off the substrate. Scale bar=100µm. **b**, WARP image sequence of larva prior to (-1.5s to -0.5s) and engaging in (0s) a headsweep (representative of 2 animals and 3 turns). Note the large posterior displacement (blue arrow). (Images cropped around the animal.) Scale bar=200µm. **c**, Profiles of cavity displacement along anteroposterior (A-P) axis in resting state (black dotted line at -1.5s in **b**) and pre-headsweep (red dotted line at -0.5s in **b**), showing that peak displacement decreased across all segments from the resting state (grey box) to pre-headsweep (pink box). **d**, Bilateral displacement profile across the mediolateral (ML) axis of the A4 protopodium (solid lines in **b**) at different times prior to the headsweep, showing that the width of the contact increases from the resting state (-1.5s) to the pre-headsweep state (-0.5s) and partially reduces again immediately after head movement. **e**, (**i**) Brightfield image (3rd instar larva) and (**ii**) displacement map (2nd instar larva) of the posterior-most body segment, showing how two cuticular protrusions (white arrowheads) and the terminal protopodium (A8) generate a tripod-shaped substrate displacement. (**iii**) Profiles along blue and red dotted lines in (ii). Scale bar=200µm (i) and 100µm (ii). **f**, Sequence of displacement maps of tripod structure before the start of a forward wave (<0.24s) and the removal of tripods upon beginning of peristalsis (>0.48s). Scale bar=100µm. **g**, Percentage of forward waves (FW), bilateralisms (BL), backward waves (BW) preceded by tripod contact, and tripod deployments without any observed locomotor behaviour (unrelated). **h**, Time delay between tripod deployment and initiation of movement at A7. Points colour-coded by animal, n=6. Line=mean, box=±1 standard error of the mean, whiskers=±1 standard deviation.

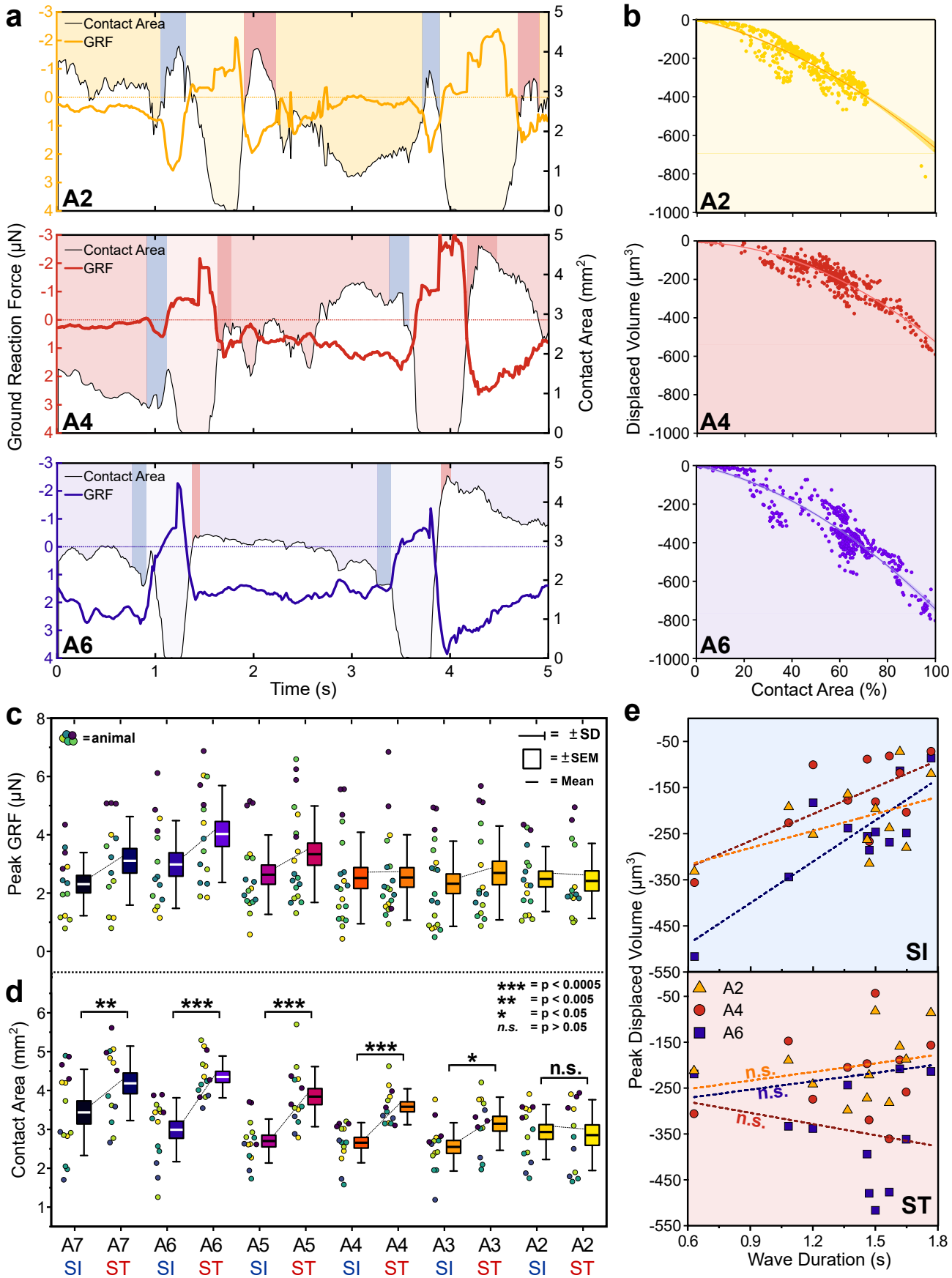
a
Contact Area
GRF
A2
A4
A6
Ground Reaction Force (μN)
Contact Area (mm²)
Time (s)
b
Displaced Volume (μm³)
Contact Area (%)
c
=animal
= ±SD
= ±SEM
= Mean
Peak GRF (μN)
d
*** = p < 0.0005
** = p < 0.005
* = p < 0.05
n.s. = p > 0.05
Contact Area (mm²)
A7 SI
A7 ST
A6 SI
A6 ST
A5 SI
A5 ST
A4 SI
A4 ST
A3 SI
A3 ST
A2 SI
A2 ST
e
SI
ST
A2
A4
A6
n.s.
Peak Displaced Volume (μm³)
Wave Duration (s)

Figure 5. Protopodia produce GRFs in the micronewton range and show complex spatiotemporal dynamics.

a, Ground reaction force (GRF, coloured line) and protopodial contact areas (white area under black line) during forward crawling for A2, A4 and A6 protopodia, showing progression of waves through animal (light-coloured boxes). Blue (SI) and pink (ST) boxes denote characteristic troughs in GRF immediately prior to protopodia leaving the substrate and returning to the substrate, respectively. **b**, Volume displaced by different protopodia show a 2nd order polynomial relationship with the contact area of that protopodium (A6: R^2=0.91, A4: R^2=0.91, A2: R^2=0.88). **c**, Peak GRFs and **d**, peak contact area during SI and ST across body segments. Data points denote single events, colours indicate different animals. n=5, 15 waves. Contact areas were compared by a two-way repeated measures ANOVA (*<0.05, **<0.005, ***<0.0005, n.s.=not significant). **e**, During SI, peak displaced volume was correlated to wave duration for larger abdominal segments (A6: R^2=0.69; A4: R^2=0.48) but not for smaller anterior segments (A2: R^2=0.24). During ST, it was not correlated regardless of the segment (A6: R^2=0.05; A4: R^2=0.05; A2: R^2=0.08). n=4, 11 waves.

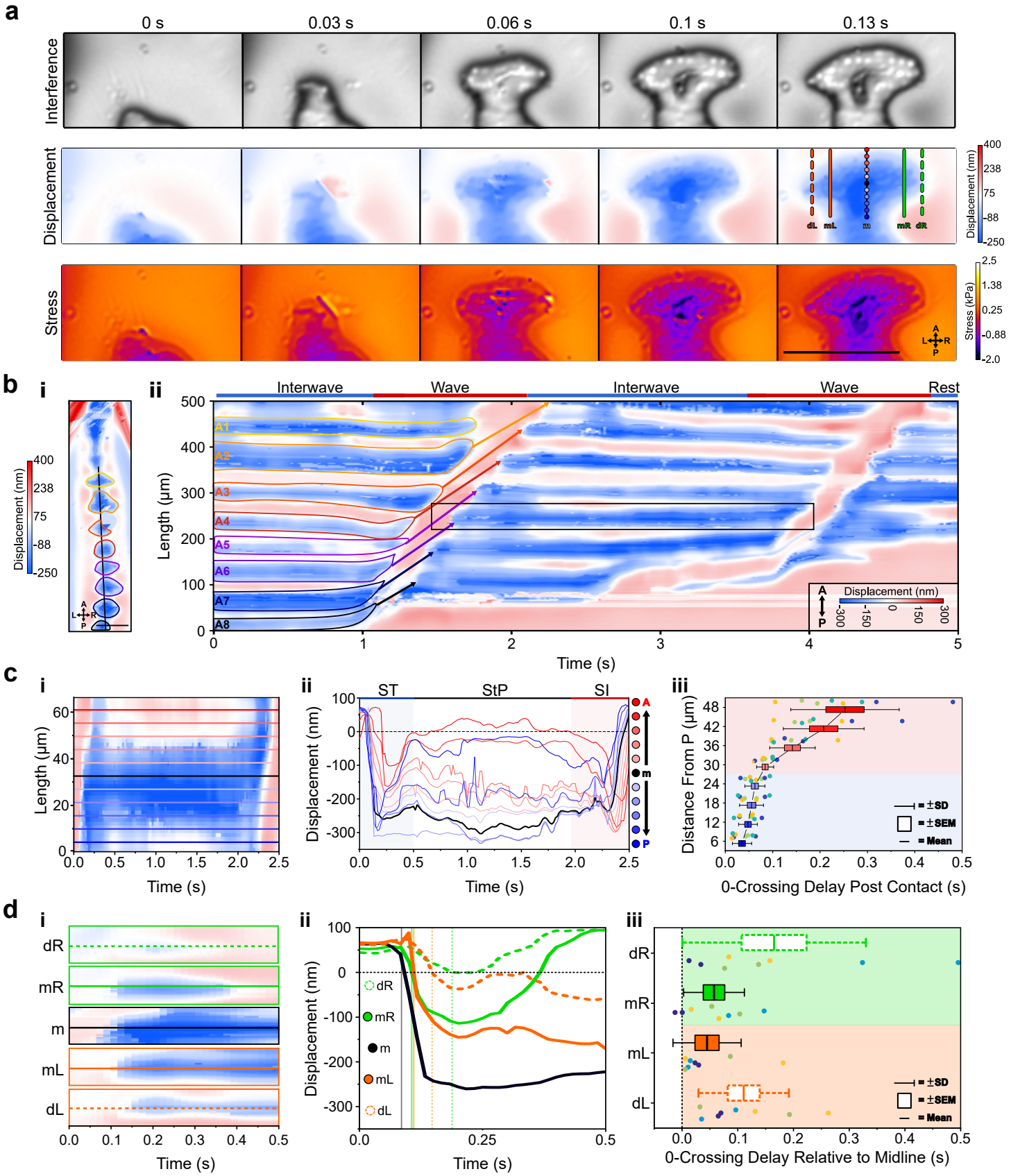
a
0 s
0.03 s
0.06 s
0.1 s
0.13 s
Interference
Displacement
Stress
dL mL m mR dR
Displacement (nm)
400
238
75
-88
-250
Stress (kPa)
2.5
1.38
0.25
-0.88
-2.0
A
L
R
P
b
i
ii
Displacement (nm)
400
238
75
-88
-250
Interwave
Wave
Interwave
Wave
Rest
Length (µm)
A1
A2
A3
A4
A5
A6
A7
A8
Displacement (nm)
-300
-150
0
150
300
Time (s)
c
i
Length (µm)
Time (s)
ii
ST
StP
SI
Displacement (nm)
Time (s)
iii
Distance From P (µm)
±SD
±SEM
Mean
0-Crossing Delay Post Contact (s)
d
i
dR
mR
m
mL
dL
Time (s)
ii
Displacement (nm)
Time (s)
iii
dR
mR
mL
dL
±SD
±SEM
Mean
0-Crossing Delay Relative to Midline (s)

Figure 6. Sub-protopodial force dynamics reveal sub-step processes and functional substrate interfacing domains in each step.

a, WARP imaging of protopodial landing during ST of an A6 protopodium. Raw interference images from WARP acquisition show footprints of individual denticles as white dots. Displacement and stress maps show how landing starts with posterior denticle rows before spreading out along the AP and ML axes. Scale bar=100µm. **b**, **(i)** Displacement map of whole animal. **(ii)** Kymograph of displacement along AP axis (black line in i) over 2 forward waves. Bands of red and blue correspond to naked cuticle and protopodia, respectively. Scale bar=100µm. **c**, (**i**) Kymograph of displacement along the AP axis of an A6 protopodium (box in **b**). (**ii**) Profiles across kymograph at different positions along the AP axis of protopodium (lines in i). (**iii**) Latency of substrate indentation (displacement <0nm) during ST along the AP axis, relative to the extreme posterior of protopodium. Compared to the posterior half of protopodium (light blue area), the anterior half shows larger latencies and variations in latency (light red area). n=4 animals, 8 swing termination events. **d**, Kymograph of displacement along AP axis during ST for the distal left (dL), medial left (mL), midline (m), medial right (mR) and distal right (dR) section of the A6 protopodium. Height of each kymograph, 66.42µm, (**ii**) Profiles across the central AP line of each kymograph in (i). Vertical lines indicate times when midline, medial right/left and distal right/left indentation starts (displacement <0nm). (**iii**) Latency of substrate indentation during ST relative to the midline for medial right/left and distal right/left locations. n=4, 8 swing termination events.

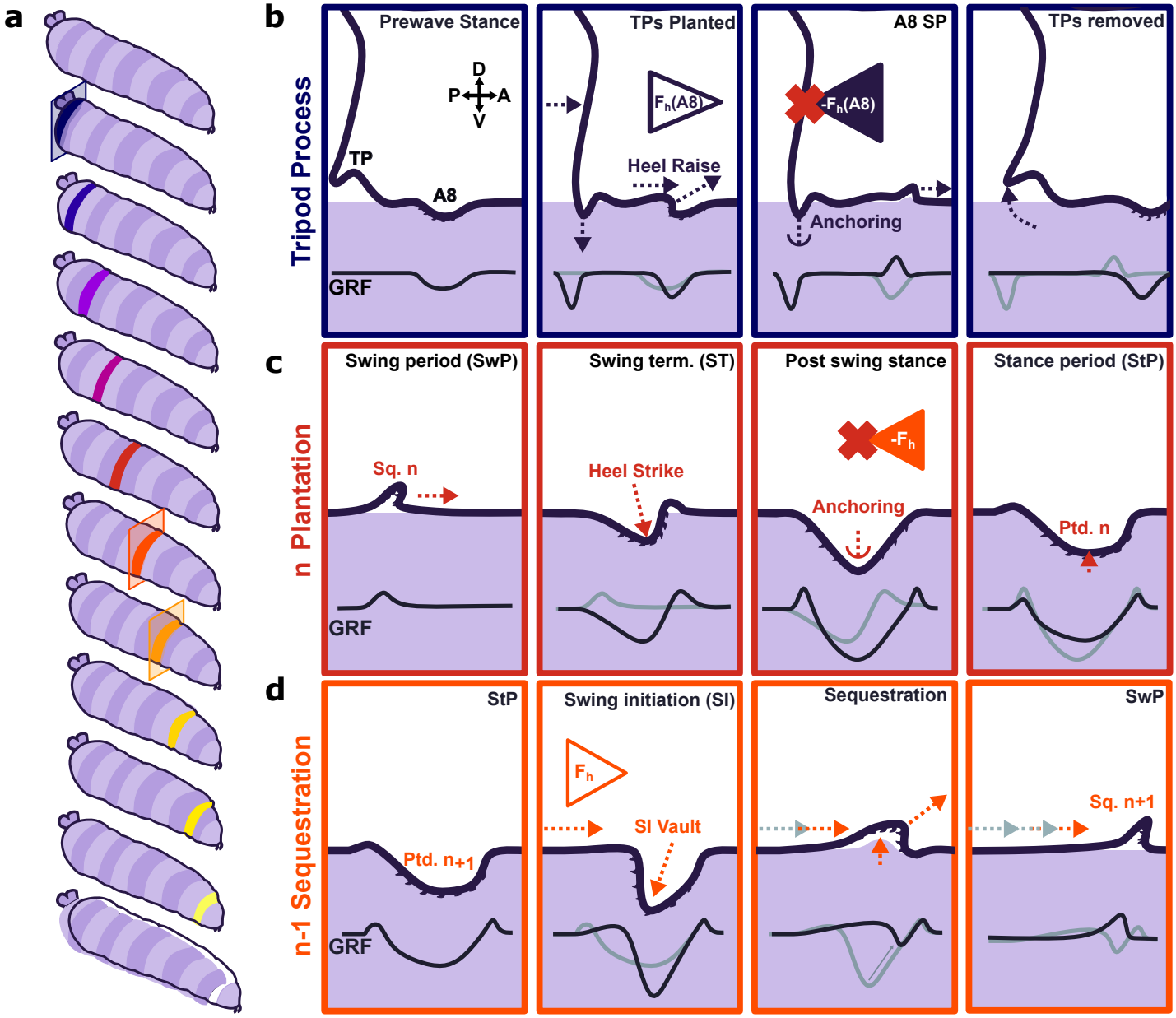
a
b
Tripod Process
Prewave Stance
D
P
A
V
TP
A8
GRF
TPs Planted
F_h(A8)
Heel Raise
A8 SP
-F_h(A8)
Anchoring
TPs removed
c
n Plantation
Swing period (SwP)
Sq. n
GRF
Swing term. (ST)
Heel Strike
Post swing stance
-F_h
Anchoring
Stance period (StP)
Ptd. n
d
n-1 Sequestration
StP
Ptd. n_{+1}
GRF
Swing initiation (SI)
F_h
SI Vault
Sequestration
SwP
Sq. n+1

Figure 7. Proposed model for protopodia-substrate interactions during *Drosophila* larval locomotion.

a, Schematic illustration of forward wave propagating from posterior (blue) to anterior (yellow). **b**, At the start of a forward wave, animals contract the posterior-most abdominal segment (A8), producing an anterograde horizontal force F_h(A8). Due to Newton's 3rd law, there is an equal but opposite reaction force -F_h(A8). To counteract this force, tripod processes (TPs) deploy onto the substrate and generate a temporary anchor, allowing the A8 protopodium to swing forward. **c**, During swing termination (ST) at the end of the swing period (SwP) of segment A*n*, the corresponding sequestered protopodium (Sq. *n*) strikes the substrate with its posterior most denticle row, then gradually unfolds into the substrate along its entire anteroposterior extent. During the stance period (StP), this planted segment *n* (Ptd. *n*) forms an anchor to mitigate the retrograde reaction force due to the subsequent contraction of segment *n*-1. **d**, In time with anchoring of protopodium *n*, protopodium *n*-1 performs swing initiation (SI) by removing denticles from the substrate and sequestering into an invagination pocket, which reduces friction during the subsequent SwP. The contraction of segment *n*-1 then leads to an anterograde force (F_h) that is balanced by the anchoring of protopodium *n* as illustrated in **c**.